Journal of Fluids and Structures 124 (2024) 104046

Contents lists available at ScienceDirect

Journal of Fluids and Structures

journal homepage: www.elsevier.com/locate/jfs

Influence of magnetically-induced nonlinear added stiffness on the lift galloping of square cylinders at low Reynolds number

Mostafa R. Rashed [a,*], Mostafa E.A. Elsayed [b], Mahmoud Shaaban [c,d]

[a] Mechanical Engineering Department, Faculty of Engineering, Modern University for Technology and Information, Cairo, Egypt
[b] Automation and Energy Technology Lab., Mechanical Engineering Department, Shoubra Faculty of Engineering, Benha University, Cairo, Egypt
[c] Mechanical Engineering Program, School of Engineering and Applied Sciences, Nile University, Giza, Egypt
[d] Smart Engineering Systems Center, Nile University, Giza, Egypt

ARTICLE INFO

Keywords:
Galloping
Square cylinder
Energy harvesting
Nonlinear stiffness

ABSTRACT

A square cylinder may gallop if subjected to fluid flow, experiencing a self-excited vibration mode that can harvest energy for low-power applications. The harvested power is typically low and depends on the upstream flow velocity and system dynamic parameters. In this study, the influence of nonlinear stiffness induced by two repulsive magnetic poles on the galloping response of square rods is investigated at a mass ratio of 10 and a Reynolds number of 200. The vibration response of two identical coaxial square rods with magnetic poles attached to their opposite ends is analyzed. Two simplified configurations are selected to model the magnetic forces: a pair of identical monopoles and a pair of identical dipoles. Results show that the magnet configuration and strength significantly affect the vibration amplitude and the onset flow velocity. A weak magnetic force can enhance vibration and reduce onset flow velocity, while a stronger pair of dipoles may push the bistable system to a state of low-amplitude vibration with a mean displacement. The influence of magnets in this configuration has potential as a control technique for energy harvesting applications.

1. Introduction

Fluid flow normal to axes of structures gives rise to phenomena of interest to scientists and engineers. Flow-induced vibration (FIV) conditions are particularly interesting and lead to increased oscillatory motion and associated forces, such as vortex-induced vibration (VIV) and galloping. Galloping has attracted significant research over decades as extensively reviewed by Parkinson (1989), Mannini et al. (2014), Wang et al. (2020), due to its typically undesirable implications for many engineering devices and structures subject to cross-flow, such as power cables (Smith, 1993; Jafari et al., 2020), marine pipelines (Faltinsen, 2014; Xia et al., 2022), slender wind turbine supports (Yin et al., 2022), nuclear reactors (Blevins, 1979), bridges (Fujino and Siringoringo, 2013), and many others (Novak, 1972). However, more recently, devices designed to induce controlled galloping are being tested for low-intensity energy harvesting (Ma and Zhou, 2022). Galloping is a divergent system instability where the structure oscillates with a high amplitude as the incoming fluid velocity increases. As an aeroelastic instability, galloping occurs when small oscillations lead to increasing fluid forces that can overcome the inherent damping of the structure. Long and slender structures of non-circular cross-sections are prone to low-frequency quasi-periodic motion excited as an onset flow velocity is exceeded. Under these conditions, such structures gallop in the transverse direction if subjected to flow normally to their axis. The subsequent increase in displacement amplitude stabilizes as the fluid damping forces balance the reduced system damping, and a limit cycle is reached.

* Corresponding author.
E-mail address: mostafa.rashed@eng.mti.edu.eg (M.R. Rashed).

https://doi.org/10.1016/j.jfluidstructs.2023.104046
Received 26 June 2023; Received in revised form 6 October 2023; Accepted 5 December 2023
Available online 21 December 2023
0889-9746/© 2023 Elsevier Ltd. All rights reserved.

List of symbols

$\mathbf{B}$	magnetic field strength vector
c	structural damping coefficient
C_B	magnetic force strength factor
C_d, C_l	drag and lift coefficients
f	frequency
$\mathbf{F}$, F	force vector and amplitude
$\mathbf{i}$, $\mathbf{j}$, $\mathbf{k}$	unit vectors in streamwise, transverse, and axial directions
k	structural stiffness
L	Cross-section edge length
m	structure mass, magnetic dipole moment
m^*	mass ratio
$\mathbf{n}$	unit vector normal to surface
P, p	absolute, normalized pressure
q	magnetic charge
$\mathbf{r}$, r	direction to charge in magnetic field; vector and amplitude
Re	Reynolds number
St	Strouhal number
u	normalized local flow velocity
U	upstream flow velocity
U_r	reduced flow velocity
y	normalized vibration displacement
$\dot{y}$	normalized vibration velocity
ρ	fluid density
μ	fluid viscosity
μ_0	space permeability constant
ω	vorticity
δt	timestep

Subscripts and superscripts

a, b	magnetic dipole index
B	magnetic field
m	magnetic
max	maximum amplitude
rms	root mean square
n	natural
r	reduced, normalized
1, 2	structure index

Abbreviations

ALE	Arbitrary Lagrangian–Eulerian
FIV	Flow-induced vibration
GCI	Grid convergence index
G,T	Calculation grid
P, S	Primary, secondary vortex street pattern
PE	Potential energy
VIV	Vortex-induced vibration

An extensive investigation has been conducted to observe and model the galloping of structures with a square cross-section to uncover the underlying mechanisms. Measurements of the response of square cylinders to cross-flow by Nakamura and Mizota (1975) showed that the frequency and phase angles suffer abrupt changes as the critical flow velocities for vortex excitation and galloping are reached. Bearman and Obasaju (1982) compared pressure fluctuations of stationary square cross-sections to those forced to vibrate transversely. Their measurements showed significantly different force coefficients and phase characteristics than those around circular cylinders. The behavior of the oscillating system is dependent on flow and structural non-dimensional

parameters. The Reynolds number and the reduced flow velocity are the main flow parameters. The transverse vibration response of a cylinder of a square cross-section with an edge length L is reported in the form of the normalized root mean square of the vibration displacement $y_{\mathrm{rms}} = \mathrm{rms}(y)/L$, along with the Strouhal number $St = fL/U$, where f is the oscillation frequency and U is the flow velocity. The motion is dominated by a number of flow and structure variables (Obasaju et al., 1990). These include the structure's natural frequency $f_n = \sqrt{k/m}/2\pi$ based on its mass m and stiffness k per unit length. The galloping amplitude increases nearly linearly with the reduced flow velocity $U_r = U/(f_n L)$ after it is initiated at an onset value. A minimum displaced mass ratio $m^* = m/\rho L^2$ is necessary for a cylinder to gallop (Sen and Mittal, 2016), and galloping is typically initiated at an onset Reynolds number that weakly depends on the mass ratio (Sen and Mittal, 2011).

Traditionally, galloping has been analyzed by means of quasi-steady analysis, where the fluid force on the structure is assumed to be dependent only on the incident angle and independent of the flow field unsteadiness (Parkinson, 1974; Landl, 1975). Early analysis by Parkinson and Brooks (1961) relied on an algebraic dependence of the lift coefficient on the incidence angle and was validated by sufficient agreement with experiments (Parkinson and Smith, 1964). Chen et al. (2021) showed that the prediction of the galloping response can be vastly improved through the use of unsteady force measurements and suggested that while the quasi-steady theory can predict classical galloping, it fails to predict galloping with the effect of vortex shedding, in which the influence of the unsteady patterns in the flow is considerable. Mannini et al. (2018) employed a wake-oscillator model that relies on the linear superposition of the unsteady wake force producing vortex-induced excitation and the quasi-steady force that is responsible for galloping. Although the model predictions are qualitatively satisfactory, the quantitative agreement with the experimental data is limited by the nonlinear features of the interaction (Dimitriadis, 2017). Joly et al. (2012) adopted a model based on the quasi-steady theory to enable the prediction of sudden changes in amplitude at low Reynolds numbers and different mass ratios. They indicated that the interaction between the oscillatory force of vortex shedding and the galloping mechanism plays an important role that can be captured in finite element simulations. Gao and Zhu (2017) showed that results predicted by quasi-steady analysis often deviate greatly from the true values due to the ignorance of unsteady effects.

Numerical models based on finite element analysis have performed well as a tool to model the mechanism of galloping, especially at low Mach and Reynolds numbers (Wanderley and Levi, 2002). Available models provide accurate predictions of nonlinear galloping systems compared to linear methods such as the quasi-steady theory and linear stability analysis, as emphasized by Li et al. (2019) who employed a numerical analysis to model the mode competition in galloping of a square cylinder at a low Reynolds number. Zhao et al. (2013) employed an arbitrary Lagrangian–Eulerian scheme to model the interaction between the vibrating cylinder and the fluid flow. They showed that the approaching angle of the flow significantly affects the vortex-induced vibration response of square cylinders. Sen and Mittal (2015) used the finite-element method to study the effect of the mass ratio on in-line and transverse free vibrations of a rigid square cylinder at Reynolds numbers ranging from 50 to 250. In contrast to predictions of the quasi-steady methods, they found that the flow around galloping cylinders is not periodic and the phase portraits exhibit quasi-periodicity under some conditions. They noted that galloping is absent below a critical mass ratio between 1 and 5 at a given blockage. Sourav and Sen (2019) later reported that the critical mass ratio value of 3.4 is required to induce galloping at Reynolds numbers higher than 250. Han and de Langre (2022) numerically solved the incompressible Navier–Stokes equation coupled with a classic mass–damper–stiffness equation and suggested that, contrary to a common statement in literature, galloping can be initiated at arbitrarily low mass ratio numbers if the necessary onset reduced flow velocity is reached.

Recently, there has been a growing interest in the use of flow-induced vibration mechanisms to provide consistent power for electronics in remote environments with abundant and sustainable flow. For instance, the increasing number of online condition monitoring and IoT applications is expected to induce a growing demand for miniature wind energy harvesters (Liu et al., 2021). The state-of-the-art and the challenges facing flow-based energy harvesting technology have been extensively reviewed in a series of articles by Hamlehdar et al. (2019), Wen et al. (2021), Ma and Zhou (2022), Cao et al. (2022), Zheng et al. (2023). Unlike the rotation-based energy harvesters, devices based on flow-induced vibration mainly transform flow energy into structural vibration via aerodynamic instability phenomena such as flutter, vortex-induced vibration, or galloping. Galloping features several advantages as a prominent mechanism for energy harvesting. For starters, there is theoretically no upper limit on the wind speed that would induce galloping, and it can be started at significantly lower wind speeds than rotation-based devices due to the absence of bearing friction (Yang et al., 2013). Moreover, the increased friction due to air drag at the miniature and nanoscales does not necessarily reduce its conversion efficiency, as air drag plays an important role in driving the conversion mechanism (Shi et al., 2020). As a result, a growing number of designs are currently in the research and development phase (Zhang et al., 2018; Ding et al., 2016; Liao et al., 2021). The incorporation of a nonlinear force into a flow-induced vibration energy harvester significantly enhances energy harvesting efficiency. Hu et al. (2022) showed that the vibration of energy harvesters can be controlled by tuning the stiffness of a secondary oscillator. Guan and Liao (2016) used nonlinear magnetic force caused by a pair of magnets to enhance the performance of a piezoelectric energy harvester. They showed that such a nonlinear configuration can be advantageous in low-frequency variable rotational motion. Mei et al. (2020) verified that a magnetic force can push an energy harvesting system into a bistable or tristable state, resulting in a performance enhancement. Zhao et al. (2014) induced nonlinear magnetic interaction between the inner and outer beams to enhance energy harvesting performance, and reported that galloping onset wind speeds could be as low as 1 m/s. Zhou et al. (2018) proposed a Y-shaped bistable energy harvester showing a coherent resonant state over a wide range of airflow speeds. Yang et al. (2019) experimentally tested a nonlinear energy harvester design with mutual magnetic repulsion force between the ends of two opposite beams. They reported an improvement in the energy output compared to an earlier iteration with one of the magnets fixed. Chen and Zhao (2023) proposed a two-degree-of-freedom structure with quasi-zero stiffness and showed that a small cubic stiffness, a small mass ratio, and a frequency ratio far away from one should be employed to avoid high onset velocities and considerable oscillations at the same time. Notably, a significant number of the aforementioned studies

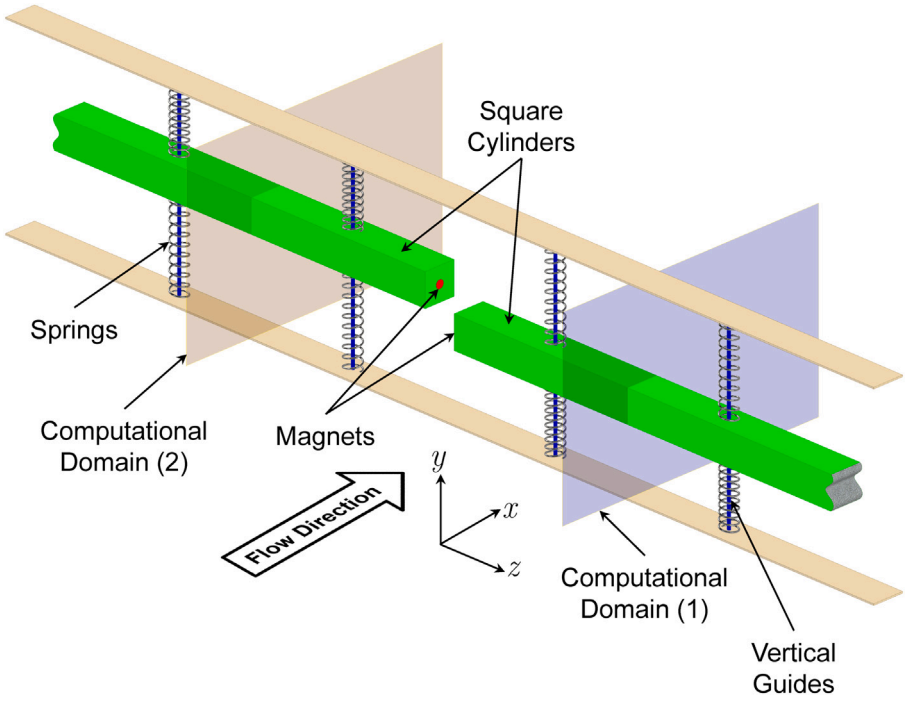


Fig. 1. A schematic of the investigated configuration.

focus on reporting an empirical improvement in harvester performance without thorough modeling of the underlying flow-structure interaction mechanisms and dynamic behavior.

The inclusion of nonlinear forces makes the dynamic characteristics of a vibrating energy harvester more complex. Accurate modeling and prediction of the nonlinear harvester performance is a persisting challenge (Ma and Zhou, 2022). In addition, nonlinear devices have been known to face chaos and bifurcation under laboratory conditions, and it is necessary to explore the influence of nonlinearity on performance and stability (Huynh and Tjahjowidodo, 2017). In nearly all designs in the published literature, nonlinear forces induce better performance in terms of power output and stability. This mounting experimental evidence of unconditional enhancement of performance is likely to be a result of fine-tuning of designs or publication bias. Identification of the mechanisms by which nonlinear forces may positively impact the performance of an energy harvester is necessary to improve and optimize designs. In addition, an accurate understanding of the nonlinear forces' effect on the performance of the galloping system can provide valuable tools for amplitude control and suppression when vibration is unfavorable.

Therefore, the objective of this work is to investigate the influence of a nonlinear magnetic force on the performance of a galloping energy harvester. A numerical flow simulation based on the incompressible Navier–Stokes equation with an arbitrary Lagrangian–Eulerian formulation coupled with a double-structure single-degree-of-freedom solver is used to study the dynamic behavior of a galloping energy harvester. The harvester design is based on two galloping objects coupled through a magnetic repulsion force. Two different configurations of the nonlinear magnetic force are investigated in the present study. The first configuration is a pair of magnetic monopoles, and the second configuration is a pair of magnetic dipoles. Both of the two configurations may induce negative stiffness close to their initial stable state. The strength of the magnetic field of the pair, and thus the strength of the repulsion force, is varied to investigate its effect on the galloping response and the dynamic stability of the system.

2. Governing equations and numerical model

A schematic of the investigated device is shown in Fig. 1. The model consists of two identical rods with a square cross-section, attached to identical springs, and allowed to move only in the transverse direction with the assistance of vertical guides. The rods are separated by a distance L, equal to the square cross-section edge length. To ensure a typical galloping response for the reference case when no magnetic nonlinear forces are applied, the mass ratio of the rods is selected to be $m^* = 10$. Moreover, the flow is laminar at a Reynolds number $Re = 200$ to eliminate the influence of the flow turbulence on the galloping response and provide a base of comparison with other studies at the same Reynolds numbers (e.g. Joly et al., 2012; Sohankar et al., 1999). The Reynolds number is kept constant while the reduced flow velocity is varied through the manipulation of the structural stiffness k, which controls the natural frequency of the system. Two identical magnetic poles are located at the center of the opposite end sections of the rods. Those poles are oriented such that they produce a repulsion force that is exactly axial when the two rods are exactly coaxial and provide repulsive force components as the rods start to oscillate.

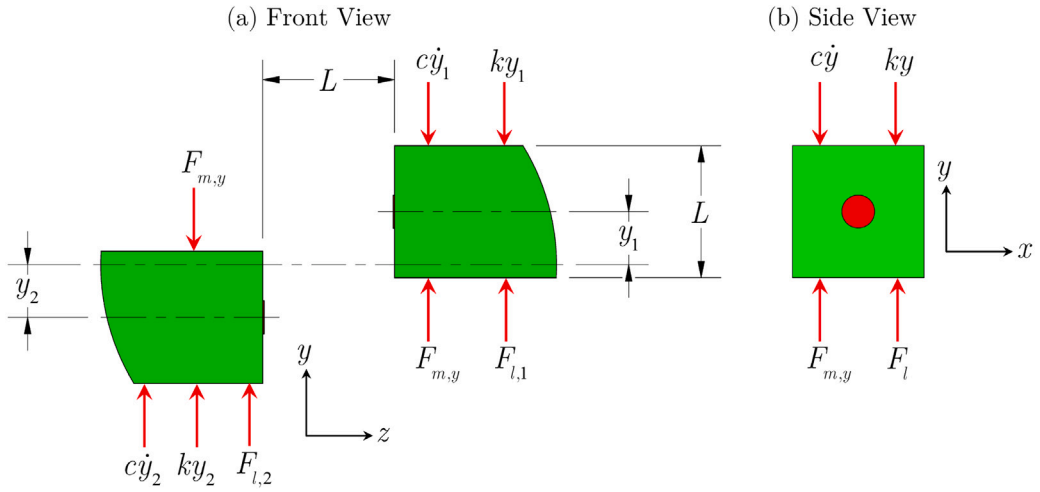


Fig. 2. The parameters of the investigated configuration and the forces acting on it in (a) the front view (parallel to the flow direction) and (b) the side view (normal to the computational domain).

2.1. Fluid–structure interaction

Because the interaction of the flow and the structural motion includes several interfering mechanisms, the standard assumptions following the analysis of Parkinson (1974) are applied to calculate the flow and structure parameters. First, the structure is allowed only to move with a single degree of freedom, assuming a high disparity between the effective stiffness in the transverse and streamwise directions (Carassale et al., 2013). Second, steady laminar flow, free of perturbation, is assumed at a zero incidence angle to the axis of the structure. Third, the structure is sufficiently long and slender to ensure that forces are dominated by the two-dimensional flow and that end effects are marginal. Finally, no structural damping is assumed to provide the upper limit of the vibration amplitude, as the structural vibration is expected to decrease with an increased damping ratio. In this work, the rods are constrained to move in a single direction. This direction is a translation of the whole body normal to the inlet flow direction and normal to the rod axis. This motion is the typical galloping direction, such that its driving force is the lift oscillating component and the transverse magnetic repulsion force component. This direction is hereby referred to as transverse. The two other possible components, namely streamwise motion driven by the drag force, and axial motion driven by the axial magnetic repulsion force component and edge fluid flow, are completely constrained by design and assumed to be eliminated through rigid fixation. Each of the two long rods is expected to move with uniform structural stiffness over its length in the transverse direction. No rotation component is allowed. This can easily be set up using linear springs attached over the rod length such that there is a significant modal disparity between the translation and rotational modes around the rod center.

For a two-dimensional square cylinder elastically supported and subjected to flow and magnetic forces, as shown in Fig. 2, the cross-flow displacement y satisfies a simple oscillator equation with mass m, damping c, and stiffness k, such that

$$m\ddot{y}_1 + c\dot{y}_1 + ky_1 = F_{m,y} + F_{l,1} \tag{1}$$

$$m\ddot{y}_2 + c\dot{y}_2 + ky_2 = F_{m,y} - F_{l,2} \tag{2}$$

where the magnetic force F_m is discussed in Section 2.2 and $F_{l,i}$ represents the effect of the lift forces on the ith cross section. To calculate F_l on each cross-section, the flow field is modeled by the transient incompressible Navier–Stokes equations in the non-dimensional Arbitrary Lagrangian–Eulerian (ALE) form (Takashi and Hughes, 1992);

$$\frac{\partial u_i}{\partial x_i} = 0 \tag{3}$$

$$\frac{\partial u_i}{\partial t} + \left(u_j - u_{g,j}\right)\frac{\partial u_i}{\partial x_j} + \frac{\partial p}{\partial x_i} = \frac{1}{\mathrm{Re}}\frac{\partial^2 u_i}{\partial x_j \partial x_j} \tag{4}$$

where u is the normalized flow velocity in the cartesian coordinates $i, j \in \{x, y\}$, and u_g is the velocity of the grid points. $p = P/\rho U^2$ is the normalized pressure. The Reynolds number in a fluid of viscosity μ is $Re = \rho U L/\mu$. Gravity is not included in the formulation of body forces for neither the flow nor the structure domain, as its deflection will be opposed by a mean spring deflection.

The computational grid used for the simulation is shown in Fig. 3, extending $20L$ upstream, $40L$ downstream, and to a width of $40L$ to provide a reasonable compromise between accuracy and computational cost as recommended by Li et al. (2019). Two quadrilateral structured grid zones of 85,000 elements each are used to independently calculate the flow field around the two square cross-sections. The grid is fully orthogonal, and the square walls are resolved by 200 elements of an aspect ratio near unity. The

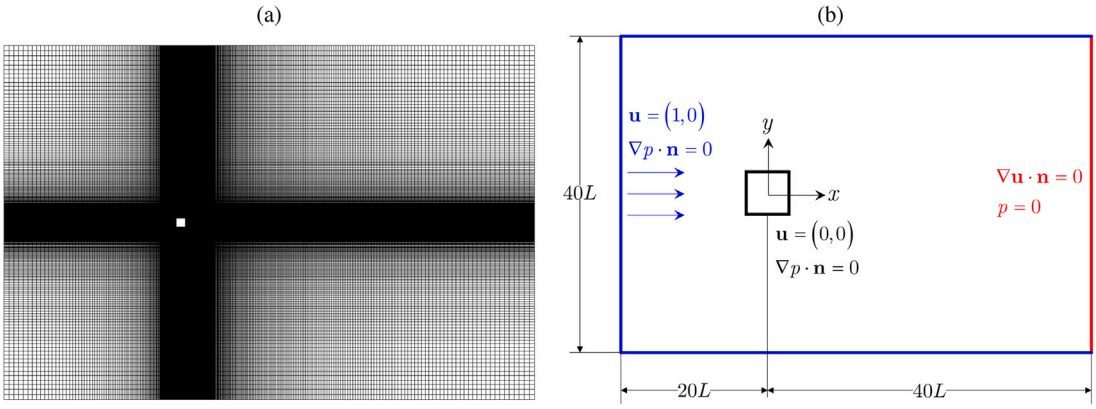


Fig. 3. (a) Computational grid configuration for the two fluid zones, and (b) the boundary conditions utilized during the present study.

Table 1
Fluid flow boundary conditions.

Boundary	Pressure	Velocity
Inlet	$\nabla p \cdot \mathbf{n} = 0$	$\mathbf{u} = (1, 0)$
Sides	$\nabla p \cdot \mathbf{n} = 0$	$\mathbf{u} = (1, 0)$
Square Walls	$\nabla p \cdot \mathbf{n} = 0$	$\mathbf{u} = (0, 0)$
Outlet	$p = 0$	$\nabla \mathbf{u} \cdot \mathbf{n} = 0$

flow field in the two zones is updated each time step such that the grid speed u_g is equal to the motion of the solid boundary as calculated from the previous time step using Eqs. (1) and (2), such that for each object, $u_g = \dot{y}_i$. As a result, no deformation of the mesh occurs and the grid quality is preserved while all mesh nodes in one zone translate uniformly in the transverse direction. For both zones, the boundary conditions shown in Fig. 3 and listed in Table 1, are applied, with different values only for the location and velocity of the square cross-section wall according to the previous time step. A fixed flow velocity condition and a zero pressure gradient condition are applied at the inlet and the sides of the domain. The outlet condition specified a reference pressure with a value that is not detrimental to the solution due to incompressibility. The walls of the square section have a no-slip condition. A pressure implicit scheme with operator splitting is used for pressure–velocity coupling by the incompressible solver. A second-order upwind spatial discretization scheme of the convective terms is used for its high stability and accuracy compared to the lower-cost first-order scheme. A least-squares discretization scheme is used to calculate gradients and a bounded second-order scheme is applied to resolve time derivatives.

2.2. Magnetic nonlinear forces

The magnetic repulsion force is calculated based on two different simplified configurations representing two ideal cases: a pair of monopoles of the same charge sign and a pair of dipoles with opposite moment directions. The repulsion force between two monopoles of equal strength q is

$$\mathbf{F}_m = q\mathbf{B} = \frac{q^2}{4\pi\mu_0 r^2}\hat{\mathbf{r}}, \tag{5}$$

where $\mathbf{r}$ is the direction vector between the two poles, $r = \sqrt{L^2 + (y_2 - y_1)^2}$ is its magnitude, and μ_0 is the permeability. Setting $C_B = q^2/4\pi\mu_0 L^3$ as a constant that represents the relative strength of the pole pair, the cross-flow force component is dependent on the location of the two squares. Eq. (6) shows that the force induced by the monopoles is a nonlinear stiffness force.

$$F_{m,y} = \mathbf{F}_m \cdot \mathbf{j} = C_B \frac{y_2 - y_1}{\left[1 + \left(\frac{y_2 - y_1}{L}\right)^2\right]^{3/2}} \tag{6}$$

Fig. 4 shows the characteristics of the transverse component of the monopole repulsion force as a function of the independent structure degrees of freedom y_1 and y_2. The upper row provides the total restoring force in the normalized form F/kL, such that F is the force affecting the structure at the location y_1. The restoring force is defined as the total force in the direction of the state $y_1 = y_2 = 0$. It consists of the spring force added to the component of the magnetic force pushing to restore the state $y_1 = y_2 = 0$. Due to symmetry, the force on the second structure at the state (y_1, y_2) is equal to the force on the first structure at the state (y_2, y_1). With no magnet, the force on y_1 is independent of y_2 due to the absence of any influence from the second square. The restoring effect of the spring is clear, as the restoring force is positive everywhere, linearly increasing as the deviation from $y_1 = 0$ increases. As the ratio of the nonlinear force factor C_B to the stiffness increases, the relative locations of the two squares start to have an effect.

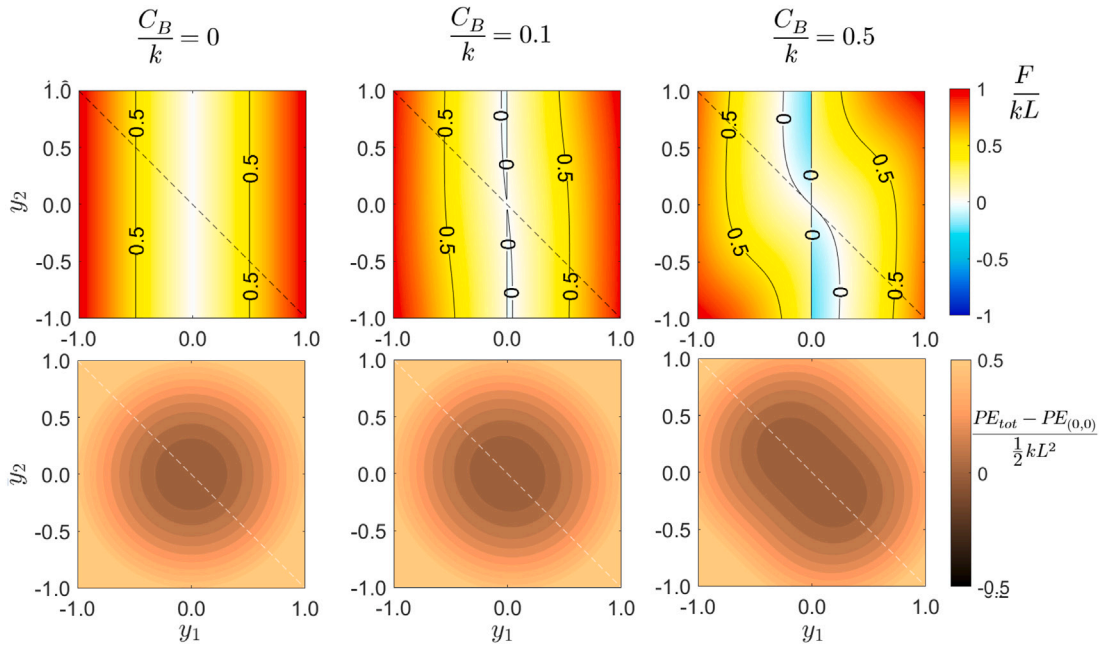


Fig. 4. The dynamic characteristics of the monopole-enhanced system show the restoring force F on the rod and the potential energy U_{tot} as a function of the two structure locations y_1 and y_2. The dashed line represents an out-of-phase state with $y_1 = -y_2$.

States with a negative restoring force, equivalent to a negative system stiffness pushing it away from its stability state, are observed when the degree of freedom y_1 is very low, such that the stiffness of the spring does not play a significant role. As the magnetic force factor C_B increases further, the states of negative stiffness extend to a higher range around the state $y_1 = 0$, suggesting that the magnetic force will have a higher effect initiating the motion away from the axis at lower reduced velocities. Notably, the dashed line, which is the state of two square sections moving completely out of phase with each other, is tangential to the region of negative stiffness, which suggests that the system moving under this condition $y_1 = -y_2$ will not have an influence of negative stiffness during its motion.

The second row of Fig. 4 shows the total potential energy PE_{tot} of the system at every state, referred to as the state $PE_{0,0}$ at $y_1 = y_2 = 0$ and normalized by $0.5kL^2$. The total energy of the system is the sum of the spring and magnetic potential energies of the two squares at each state. With no magnet, the system energy is symmetric around the state $y_1 = y_2 = 0$, where total potential energy is at a minimum, suggesting that this is a stable condition for the system. Because y_1 and y_2 are completely independent, this symmetry indicates that each degree of freedom will try to reach its stable state irrespective of the state of the other, as expected. As the magnetic force increases, the total potential energy stays in a single minimum state at $y_1 = y_2 = 0$, but the field becomes elongated around the line $y_1 = -y_2$, such that the system will attempt to fall into an out-of-phase behavior between the two structures. This tendency is expected to be more dominant in stronger magnetic fields.

The other magnetic configuration represents the case when two magnets are located such that their separating distance r is much larger than their dimensions, and thus both magnets can be modeled as magnetic dipoles. The outside field of uniformly magnetized spherical magnets is exactly a dipole field (Lehner, 2010). An expression for the force between two opposite dipole moments is derived by Yung et al. (1998). The magnetic field generated by a dipole of moment $\mathbf{m}_a$ at the location of a dipole of moment $\mathbf{m}_b$ is given by:

$$\mathbf{B} = -\frac{\mu_0}{4\pi r^3}\nabla \times (\mathbf{m}_a \times \mathbf{r}) \tag{7}$$

The force exerted by dipole a on dipole b is

$$\mathbf{F_m} = \frac{3\mu_0 m_a m_b}{4\pi r^4}\left[(\hat{\mathbf{m}}_a \cdot \hat{\mathbf{m}}_b)\hat{\mathbf{r}} + (\hat{\mathbf{r}} \cdot \hat{\mathbf{m}}_b)\hat{\mathbf{m}}_a + (\hat{\mathbf{r}} \cdot \hat{\mathbf{m}}_a)\hat{\mathbf{m}}_b - 5(\hat{\mathbf{r}} \cdot \hat{\mathbf{m}}_a)(\hat{\mathbf{r}} \cdot \hat{\mathbf{m}}_b)\hat{\mathbf{r}}\right] \tag{8}$$

The dipole moments used are $\mathbf{m}_a = m\mathbf{i}$ and $\mathbf{m}_b = -m\mathbf{i}$, with a direction vector $\mathbf{r}_{ab} = -\mathbf{r}_{ba} = L\mathbf{i} + (y_1 - y_2)\mathbf{j}$. Therefore, the force vector is

$$\mathbf{F}_m = \frac{3\mu_0 m^2}{4\pi r^5}\left[\left(-3L + \frac{5L^3}{r^2}\right)\mathbf{i} + (y_2 - y_1)\left(\frac{5L^2}{r^2} - 1\right)\mathbf{j}\right] \tag{9}$$

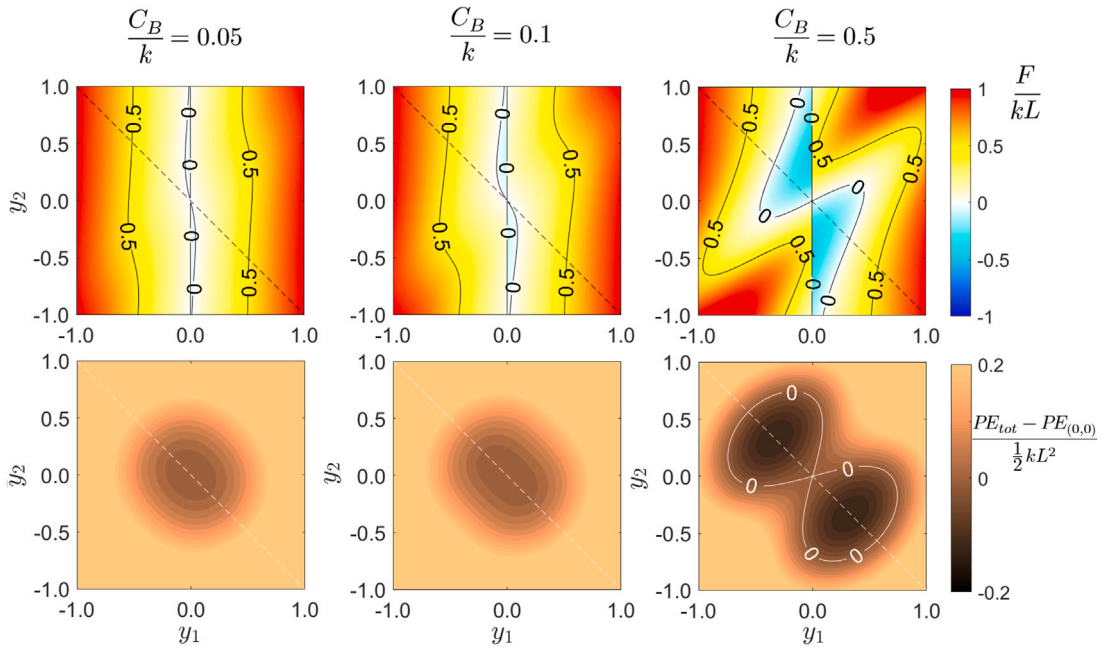


Fig. 5. The dynamic characteristics of the dipole-enhanced system, showing the restoring force F on the rod and the potential energy U_{tot} as a function of the two structure locations y_1 and y_2.

The component aligned with the direction unit vector **i** is axial, constrained by the rod supports. It is the cross-flow component that participates in the galloping mechanism of the square cylinder, with a magnitude of:

$$\begin{aligned} F_m &= \frac{3\mu_0 m^2}{4\pi r^5}(y_2 - y_1)\left(\frac{5L^2}{r^2} - 1\right) \\ &= C_B \frac{y_2 - y_1}{r^5}\left(\frac{5L^2}{r^2} - 1\right) \end{aligned} \tag{10}$$

where C_B is a constant that represents the relative strength of the dipole pair. It can be seen from Eq. (10) that the force is not always a repulsion. In fact, the force can turn into an attraction force under the condition that $5L^2 < r^2$, which is equivalent to $y_1 - y_2 < 2L$. Therefore, it is expected that the dipole pair attempts to lead the position of the two structures to that stable position if its stiffness is sufficient relative to the structure stiffness k and the fluid-added stiffness. This can also be concluded from inspecting the potential energy of each dipole due to the magnetic field of the other, U_m, the derivative of which is zero at $y_1 - y_2 = 2L$.

$$PE_m = -\mathbf{m}\cdot\mathbf{B} = \frac{\mu_0 m^2}{4\pi}\left[\frac{3L^2}{r^5} - \frac{1}{r^3}\right] \tag{11}$$

The dynamic characteristics of the dipole repulsive force in Fig. 5 show notable changes compared to the monopole dynamics. For the lower magnetic factor C_B, the dipole system behaves in a manner similar to the weak monopole system in Fig. 4. States with a negative stiffness occur at small deviations from the state $y_1 = 0$ and the out-of-phase states $y_1 = -y_2$ do not suffer the effects of this negative stiffness. The system's total potential energy shows a tendency for the system towards an out-of-phase condition. However, for the significant magnetic factor $C_B = 0.5$, the negative stiffness occurs for a wide range of states and intersects the out-of-phase states. Most importantly, the total energy of the system shows two minima, indicating a bi-stable condition where the system tends to stabilize around two different states, one of which, $y_1 = y_2 = 0$ is unstable.

The solver follows the steps in Fig. 6. From the previous time step or the initial conditions, the solver is supplied with the flow field quantities along with the location and velocity of the two cross-sections. An iterative flow solver uses these pieces of information to determine the pressure field around the structure and provides the updated flow field as an output, which is then used by the structural solver. The locations of the structures are also used to determine the transverse component of the magnetic repulsion force, which is also required by the structural solver. The structural solver calculates the transverse forces applied to the cross sections and updates their velocity and location for use in the next time step. The process continues until a statistically steady oscillating behavior is observed for sufficient time to enable the calculation of the spectral domain.

2.3. Model validation

The spatial grid convergence is verified according to the method suggested by Roache (1997) and recommended by ASME (2009) and Eça et al. (2020). The Grid Convergence Index (GCI) is established on the basis of a grid refinement error estimator derived from

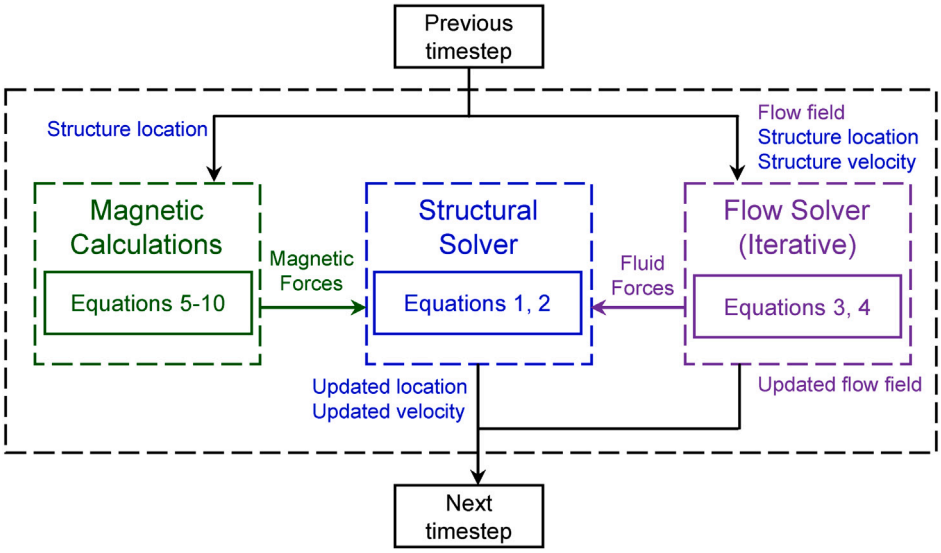


Fig. 6. The employed solver algorithm.

Table 2
Grid convergence study for a stationary square cylinder at $Re = 200$.

Grid	Number of elements	Normalized grid spacing	C_d	GCI
G1	27,500	0.299	1.53	
G2	85,000	0.170	1.47	2.44%
G3	192,000	0.113	1.46	1.16%

Table 3
Time-step sensitivity analysis.

Grid	Number of elements	δt (s)	C_d
T1	85,000	0.1	1.47
T2	85,000	0.05	1.47
T3	85,000	0.03	1.47

the theory of generalized Richardson extrapolation to provide a quantifiable measure of uncertainty regarding the convergence of the grid. The GCI serves as an indicator of the percentage deviation of the calculated value from the value of the asymptotic numerical value. Three grid configurations G1, G2, and G3, listed in Table 2, were utilized to calculate the GCI. According to the GCI study, the grid configuration G2 provided sufficient results with an error of 1.16%.

Furthermore, to ensure the reliability of the computational model, an additional sensitivity analysis was conducted to assess the impact of different time-step configurations on the obtained results. Three time-step configurations, labeled T1, T2, and T3, were examined, and their findings have been summarized in Table 3. Although the results demonstrated a high level of convergence, the T2 configuration was selected to accurately capture the vibration time signal during the current study.

The results of the model are validated against data available for square cylinders at the same Reynolds number. Table 4 shows the oscillating lift coefficient, the Strouhal number, and the mean drag coefficient for a stationary square cylinder at no incidence angle, for $Re = 200$. The results of the model used in the current study provide values in reasonable agreement with the available data. To validate the structural motion algorithm, the galloping response in terms of the root mean square amplitude is compared with the data of Li et al. (2019) which is available for $Re = 150$ and $m^* = 10$. Fig. 7(a) shows that the model accurately captures the oscillation amplitude and the onset flow velocity for both the vortex-induced vibration and the galloping mechanisms. Another validation study was carried out during the present study with the vibration maximum amplitude results of He et al. (2012) at $Re = 250$ for different values of $m^* = 10$, 20, and 40. The results showed quite acceptable agreement, as shown in Fig. 7(b).

3. Vibration response under nonlinear force influence

In this section, the effect of the nonlinear magnetic force on the vibration response, the motion of the two structures, and the associated flow field are discussed. Fig. 8 represents the time signal of the two vibrating structures after they reached statistically

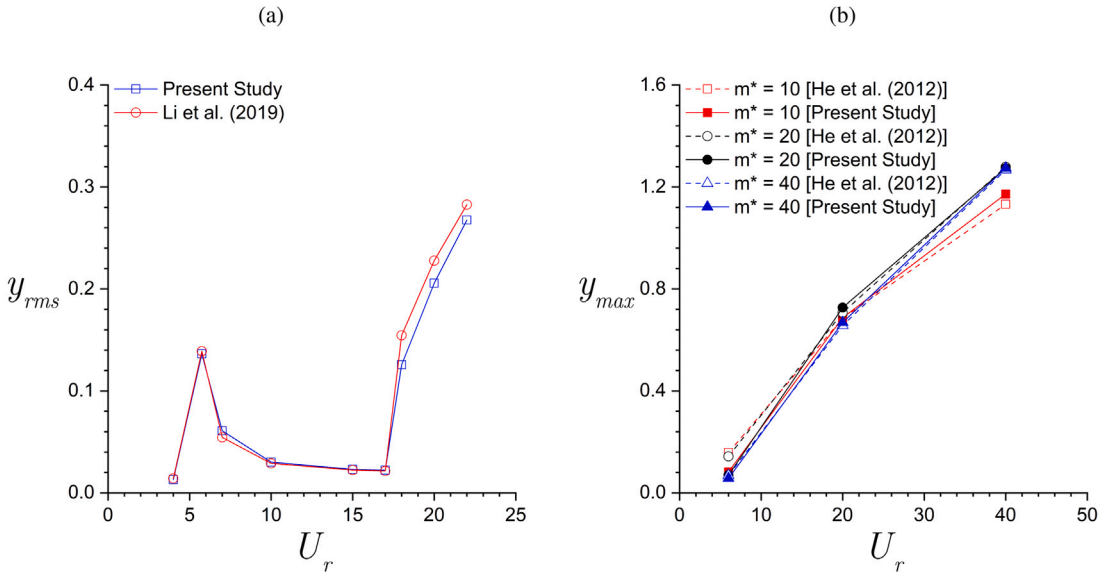


Fig. 7. (a) Root mean square vibration amplitude (y_{rms}) vs. reduced velocity (U_r) of a square rod cylinder at $Re = 150$ and $m^* = 10$ compared to the results of Li et al. (2019), and (b) maximum vibration amplitude (y_{max}) vs. reduced velocity (U_r) of a square rod cylinder at $Re = 250$ and $m^* = 10$, 20, and 40 compared to the results of He et al. (2012).

Table 4
Force coefficients and Strouhal numbers for a stationary square cylinder at $Re = 200$.

Ref.	$C_{L,rms}$	St	C_d
Present study	0.47	0.149	1.47
Joly et al. (2012)	0.42	0.151	1.44
Sohankar et al. (1999)	0.32	0.170	1.46
Singh et al. (2009)	0.55	0.142	1.54

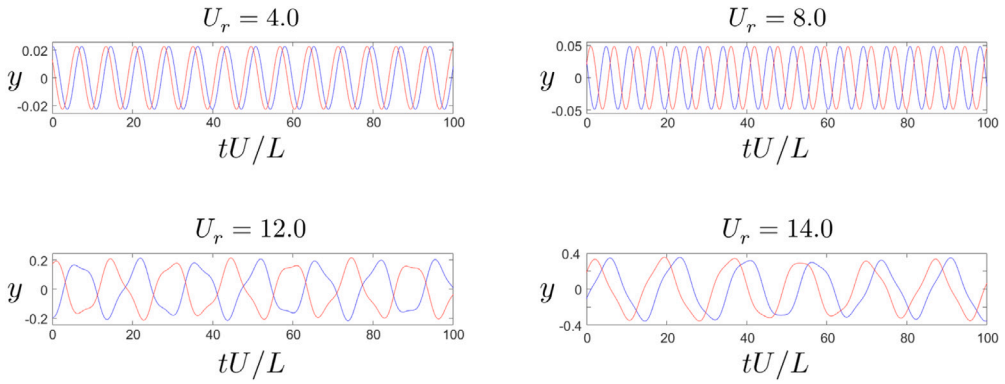


Fig. 8. The location of the two structures over time with no nonlinear force applied.

steady conditions when no nonlinear magnetic force is applied. The time signals are shown for four different reduced flow velocities to compare the motion during vortex-induced vibration at $U_r = 4.0$, directly before galloping onset at $U_r = 8.0$, and galloping at $U_r = 12.0$ and 14.0 to illustrate the effect of velocity increase. The vortex-induced vibration peak occurs around $U_r = 5.0$. The amplitude of the vibration displacement signal at $U_r = 8.0$ is slightly higher than the amplitude at $U_r = 4.0$. The normalized frequency $St = fL/U$ of the signal is increased at $U_r = 8.0$ compared with $U_r = 4.0$. At higher reduced velocities, the amplitude of the vibration displacement shows a persistent increase. On the other hand, the Strouhal number decreased significantly as the reduced velocity U_r increased, indicating the initiation of the low-frequency galloping mechanism. The signal is periodic in all cases and purely sinusoidal for $U_r = 4.0$ and 8.0. At $U_r = 12.0$ and 14.0, the signal is of an irregular pattern as a result of lift force variation at different velocities of the square cross-section in the flow field. With no magnetic force, the two structures are not

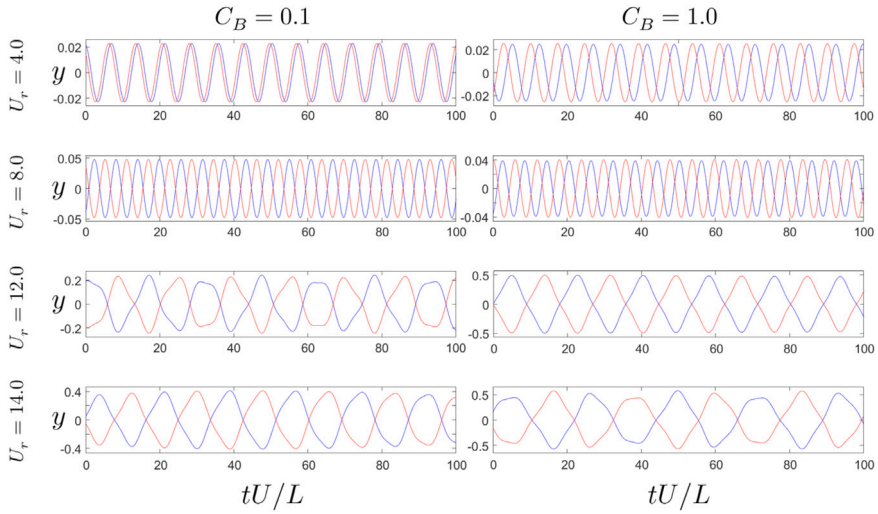


Fig. 9. Vibration time signal of the two structures with nonlinear monopole magnetic effect.

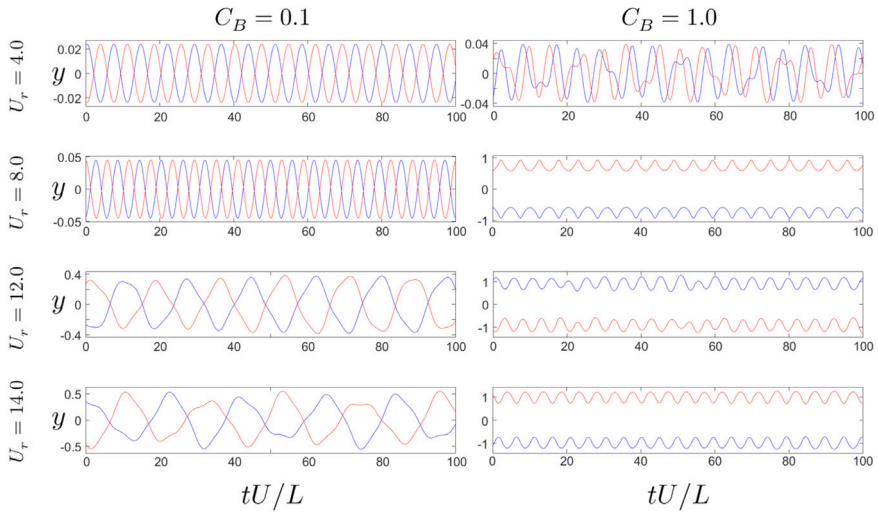


Fig. 10. Vibration time-signal of the two structures with nonlinear dipole magnetic effect.

coupled together, and their phase is randomly set by the numerical solver, and there is no tendency towards any particular phase, which is verified in Fig. 4 for $C_B = 0$.

The effect of the nonlinear repulsive force induced by a pair of magnetic monopoles on the vibration time signals of the two structures is illustrated in Fig. 9. The study was carried out on two different magnetic strengths $C_B = 0.1$, and 1.0. No significant effect of the monopole compared to the results in Fig. 8 is observed for low reduced velocities, demonstrating that the low energy in the upstream flow is not sufficient to initiate any significant effect of the square. At galloping conditions, monopoles with a magnetic strength of $C_B = 0.1$ induce a slightly higher motion amplitude than those without repulsive forces. This effect is more pronounced for monopoles with a higher strength of $C_B = 1.0$ which increased the motion's root mean square significantly, especially at $U_r = 12.0$. Notably, the vibration signal of the two structures had a random phase with each other at low reduced velocities. As the reduced velocity increases, the two structures tend towards a phase difference of 180°, in agreement with the condition of the minimum total potential energy of the system as discussed in Fig. 4.

Fig. 10 shows the motion of the vibrating structures with a pair of magnetic dipoles attached to their ends with two different magnetic strengths $C_B = 0.1$, and 1.0. The vibration signal with the lower magnetic strength does not show a significant effect except for the noted increase of the Strouhal number at $U_r = 4.0$. Nevertheless, the vibration response of the two structures utilizing the higher magnetic strength dipoles, $C_B = 1.0$, is evidently different. While the signal amplitude is not yet significant, the vibration signal at $U_r = 4.0$ deviates from the sinusoidal pattern and is not cyclic, suggesting that the strong influence of the magnetic force induced multiple motion frequencies and phases. At higher reduced velocities, the system shifts to its second stability pattern, with

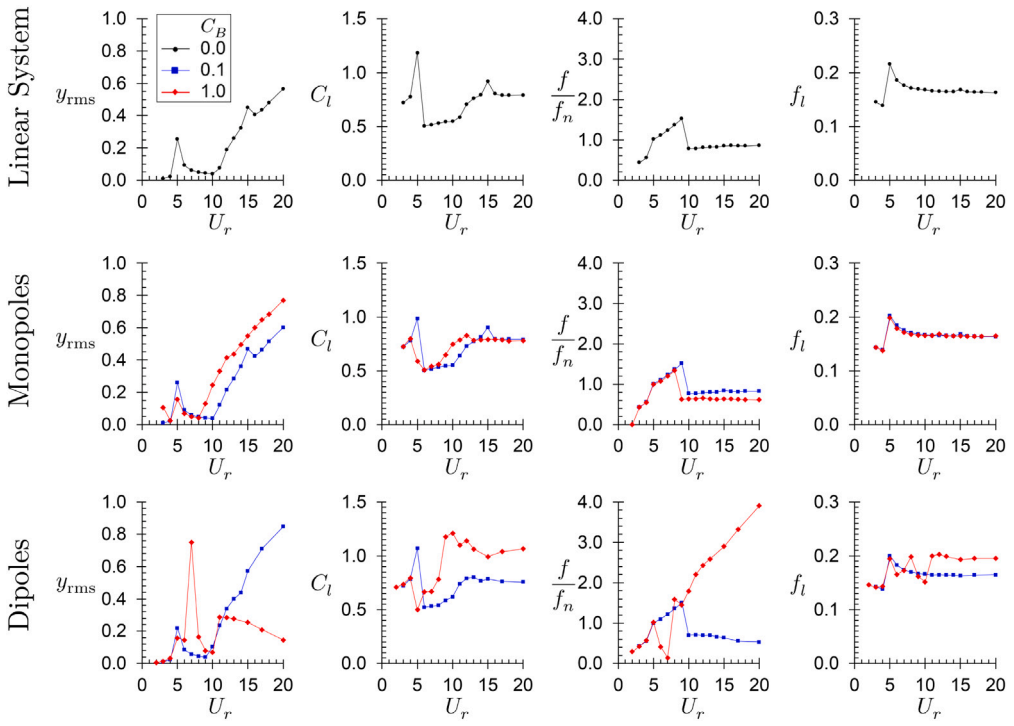


Fig. 11. Effect of reduced flow velocity U_r on the flow-induced vibration characteristics response for different repulsive force configurations.

the two structures moving in a more regularly periodic pattern, separated by a mean distance. In addition to this bistable behavior, the shifted motion is not sinusoidal, as the force is not symmetric around the new mean positions of the squares.

Fig. 11 presents the effect of the reduced flow velocity on the flow-induced vibration response for the three cases under consideration, namely; a system with a linear spring only, a system with a pair of monopoles, and a system with a pair of dipoles. In each case, two different magnetic strength factors C_B are used for each case. The first column from the lift in Fig. 11, showing the root mean square of the displacement y_{rms}, indicates that vortex-induced vibration lock-in occurred near $U_r = 5.0$ for all systems. The onset of galloping, indicated by an abrupt increase in flow velocity that persists at higher velocities, starts at $U_r = 10.0$ for the linear system. The repulsive forces of the monopoles with higher strength $C_B = 1.0$ influenced the onset of galloping to occur slightly earlier at around $U_r = 8.0$. The influence of the magnetic strength of monopoles on y_{rms} increases with the increase of the magnetic strength. In contrast, magnetic dipoles induced a different response. A remarkable increase in vibration amplitude was observed nearly after the VIV lock-in for the stronger magnetic strength factor $C_B = 1.0$, which then decreased drastically just before galloping. For $U_r = 11.0$ to $U_r = 20.0$, the vibration amplitude showed a decrease with the increase of the reduced velocity, unlike all other cases.

The dependency of the oscillating lift coefficient C_l on the reduced velocity U_r is shown in the second column of Fig. 11. As expected, the maximum value of the oscillating lift coefficient occurs near the resonance velocity for most systems due to the lock-in condition of vortex shedding with the resonant structural mode. For the magnetic dipoles with the higher magnetic strength factor $C_B = 1.0$, the lift coefficient of the square structures recorded its maximum value at the beginning of galloping near $U_r = 10.0$. This was associated with the condition of the two structures oscillating at a mean distance. In this case, the structure's motion is dictated by the repulsive forces rather than the fluid lift force and vibrates at a higher frequency than that of galloping. The higher frequency results in a higher oscillating motion velocity, increasing the lift force.

The ratio of the motion frequency to the natural frequency of the system is shown in the third column of Fig. 11. This ratio is used to distinguish the galloping mechanism's occurrence, as the frequency stabilizes at a lower value than its previous increasing trend associated with vortex-induced vibration over the galloping range of reduced velocity. This is evident for the linear system, where the frequency ratio drops to f/f_n around 0.85 at reduced velocities above onset $U_r = 10$, after its increase at lower reduced velocities. The system is influenced by monopole repulsion forces, and with the weak monopole, forces behave similarly, although the increased magnet strength results in a decrease in the frequency ratio, associated with the increased negative stiffness, as explained by the behavior discussed below in Fig. 13. For the system with strong dipole repulsion forces $C_B = 1.0$, the frequency increase does not stop beyond $U_r = 10$ but rather continues in a trend completely different from that for galloping. The increase in frequency as the structures oscillate around their new equilibrium positions, separated by a mean distance, is likely associated with an increase in the effective system stiffness at this new condition.

The fourth column of Fig. 11 includes the frequency of the lift force. For a linear system, the lift force frequency increases to a maximum at the VIV peak and then decreases to a stable value around 0.15 which is the typical vortex shedding frequency

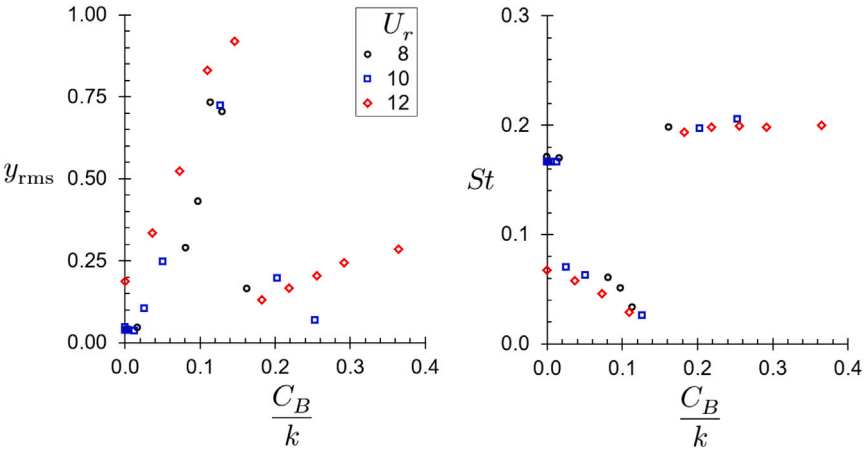


Fig. 12. Effect of dipole strength factor C_B on the (a) vibration displacement and (b) Strouhal number of square rods at three different reduced velocities within the galloping range.

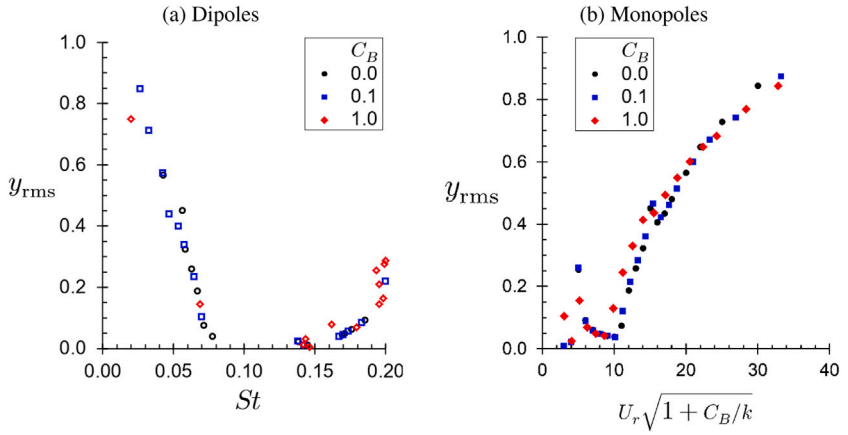


Fig. 13. (a) Vibration displacement relationship with the vibration Strouhal number at different dipole strength factors and reduced flow velocities ranging from 2 to 20, and (b) Square structures vibration response using monopole repulsive magnets at $Re = 200$, and $m^* = 10$.

downstream of square cylinders The system influenced by monopole repulsive forces did not show a significant change in the frequency of the lift force, indicating that the fluid force is not affected by the coupling. On the other hand, the higher frequency of the lift force on the structure when influenced by coupled dipoles at $C_B = 1.0$ is an indication of the dominant magnetic forces that separate the two structures, leading to a higher vibration frequency. The different behavior of the structures when separated by a mean distance indicates that this motion is not dominated by the flow force, but rather by an exchange of energy between the magnetic stiffness and the structural stiffness.

For systems with dipole repulsion forces, the ratio of the magnetic strength factor to the spring stiffness is a determining variable. Fig. 12 demonstrates the influence of C_B/k on the vibration response at three different reduced velocities within the galloping phase, namely; U_r=8.0, 10.0, and 12.0. For ratios $C_B/k < 0.15$, the amplitude of galloping increases linearly with the magnetic strength factor at all reduced flow velocities. In addition, the increase occurs at the same rate, indicating that the additional oscillating energy originates from the same mechanism. This increase falls suddenly, and the amplitude is depressed to lower values for $C_B/k > 0.15$, which are all cases where the two structures are separated by a mean displacement, as seen in Fig. 10. An increase is still gained by increasing the magnetic strength, albeit at a much lower rate. As seen from Fig. 12, the Strouhal number dependency on C_B/k passes through three stages. The inclusion of a magnet quickly reduces the Strouhal number, depressing it to nearly zero. The decrease in the oscillation frequency indicates that the magnets induce an increase in oscillation displacement through negative stiffness. Once the structures fall to their separated stable positions, the Strouhal number increases back to its original trend, suggesting that the negative stiffness is subdued and a nonlinear stiffness trend controls the vibration.

The negative stiffness effect has a significant effect on the amplitude, as evident from Fig. 13a. The figure shows that within the reduced Strouhal number range below 0.1, the amplitude of vibration is inversely proportional to the frequency. This is true for all magnetic strength factor values and also for the case with no magnet, which shows that this behavior is independent of the mechanism by which the stiffness is determined. For higher Strouhal number values, the amplitude starts to increase slightly

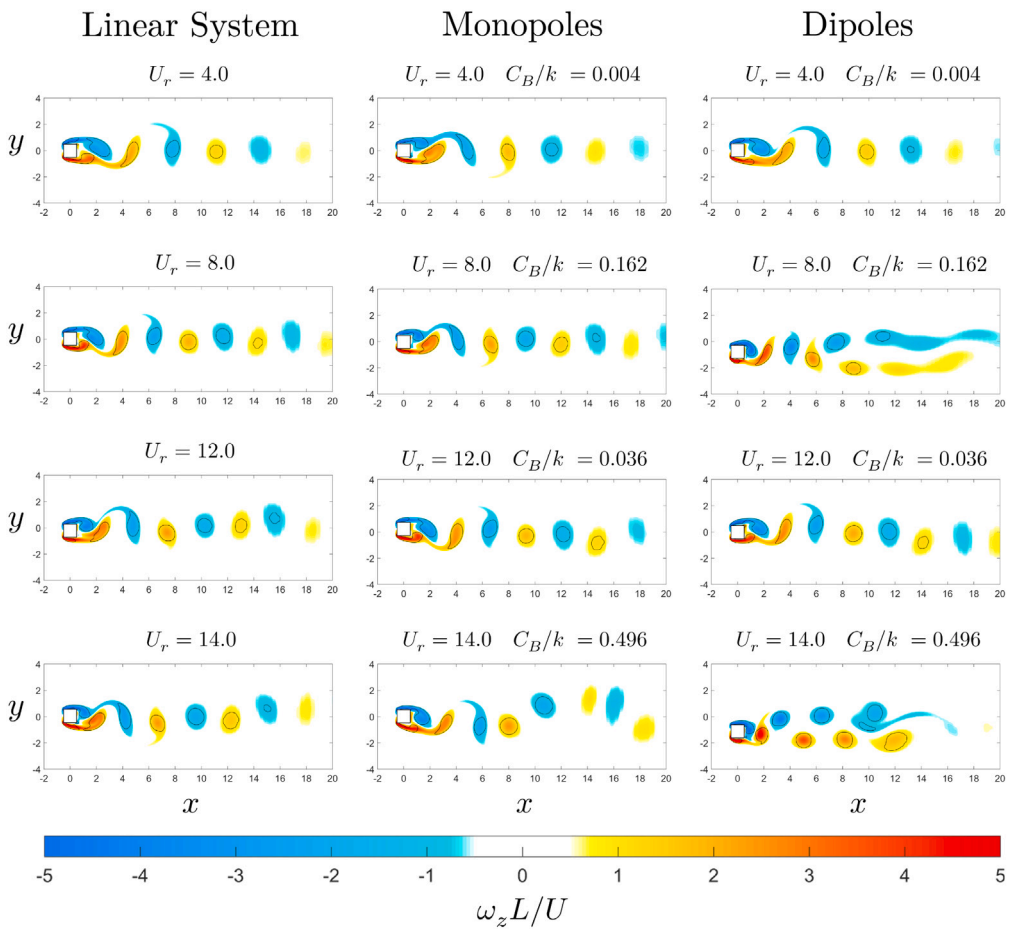


Fig. 14. Instantaneous normalized vorticity fields for the flow past the vibrating square cylinder for different linear and nonlinear systems.

and retains its lowest values around $St = 0.15$ which occurs at the lock-in range of VIV. The increased amplitude values at higher Strouhal numbers, which only occur for nonlinear systems, indicate that a different mechanism was involved, which is likely to involve the bistability mode of the structures as they oscillate around their separated stable position.

In contrast, Fig. 13b shows the galloping response of the system at three different monopole strength factors as a function of the modified reduced velocity $U_r\sqrt{1+C_B/k}$. This modified version of U_r is equivalent to the reduced velocity of a linear system with the sum of the structural stiffness and the magnet stiffness around the stable location, without including the nonlinearity. At modified reduced velocities higher than the galloping onset, the amplitude of the system is in good agreement for the three systems, showing that this modification to the stiffness is sufficient to capture the dynamics of the system. This behavior suggests that the response is dominated by the exchange of energy between the kinetic energy and the potential energy in the stiffness, and there is no considerable exchange of energy between the two forms of stiffness, magnetic and structural, on the dynamic stability of the system.

The cross-flow characteristics around the cross-section of the structures play an important role in the mechanism by which energy is exchanged between the flow and the structural vibration mode, as different vortex structures can interact differently in the wake, inducing different forces (Williamson and Roshko, 1988). To identify the flow patterns associated with the modified system behavior when nonlinear forces are involved, Fig. 14 shows a comparison between the vortex formation patterns around one of the vibrating structures. Results at four different reduced velocities are illustrated in the figure, namely, $U_r = 4.0$, 8.0, 12.0, and 14.0. It was observed that the pattern around the two structures is similar for all cases, which is expected due to the similar fluid forces, vibration amplitudes, and coupled magnetic forces that differ only in phase. Therefore, the flow field for each case is shown for one of the two structures for brevity. The flow field around the square cross-section, which is not subject to nonlinear magnetic forces, induces the formation of a 2S vortex pattern at all reduced flow velocities. As the reduced flow velocity increases, the number of vortex cores per unit length increases in the wake as they shed at a higher frequency. Due to the low amplitudes, the vortex cores are nearly aligned on the cylinder downstream symmetry line. The flow field around structures influenced by a monopole repulsive force is not significantly different at the lower reduced velocities. However, the formation of a 2P+2S vortex shedding pattern in the wake is observed at the reduced velocity $U_r = 14$ due to the significant effect of the vibrating structure motion. On the other

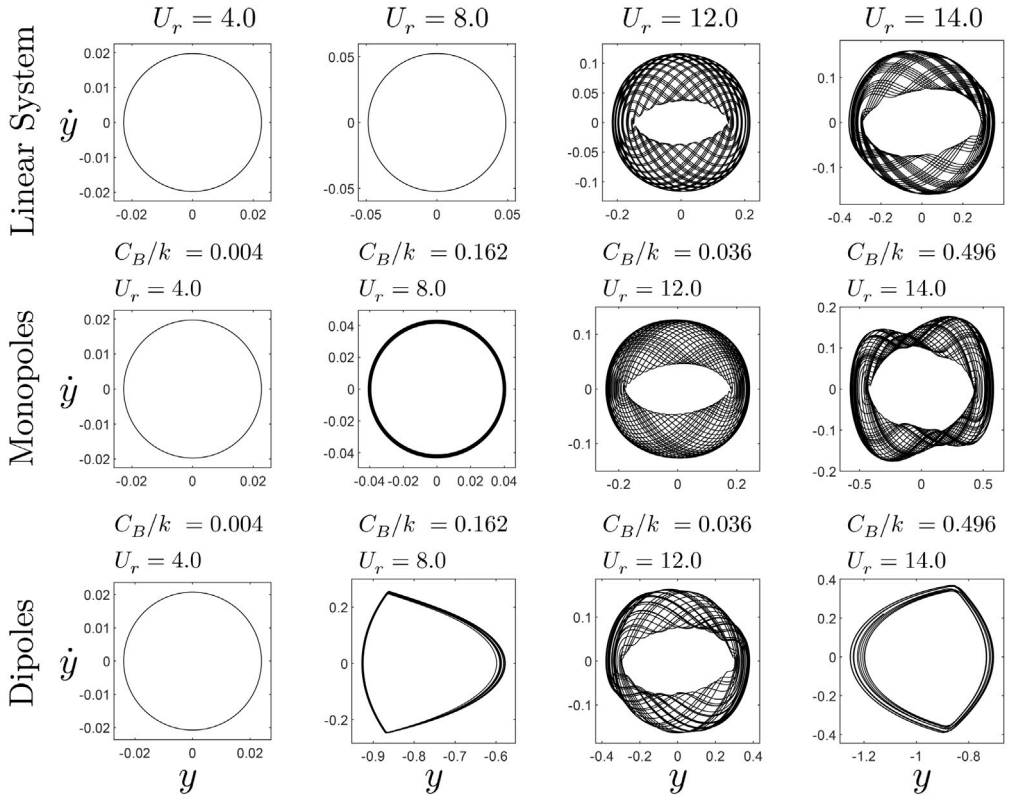


Fig. 15. Phase portraits of the transverse displacement y and the transverse velocity $\dot{y}$.

hand, structures influenced by dipoles have a notably different shedding pattern at higher reduced velocities. The pattern of 2P is observed in the wakes of the structures as they vibrate at higher frequencies and with a mean separation distance. Moreover, the asymmetric vibration around the average position induces vortex cores of different sizes and strengths at the two sides of the wake, leading to the distortion of the vorticity field further downstream.

In Fig. 15, the phase portraits for the three force configurations at different reduced velocities are illustrated. At low reduced velocities, the circular phase portrait demonstrates that the system is a periodic, single-frequency system with a stable phase between the fields that exchange energy. While both the linear system and the system influenced by monopole repulsive forces retain this periodicity up to a reduced flow velocity of $U_r = 8.0$, the system under the influence of dipoles switches to a periodic non-symmetric pattern where the kinetic energy is not symmetric around the two sides of the average position. This behavior points to an effect of the magnetic field energy exchange with the structural stiffness, which leads to the asymmetry of the kinetic energy, which does not oscillate to equal values on the two sides. The increase of the reduced flow velocity to 12 and higher leads to pseudo-periodic motion patterns. In these patterns, the structure repeats its motion over a large number of smaller cycles that are bounded by an inner and outer envelope. These envelopes represent the extreme states of the system that are possible with an energy content that is variable due to variations in the energy exchange with the flow field during the motion. This is a document characteristic of galloping dynamics and can be observed with and without the influence of magnetic forces. It is noteworthy that the adherence of the structure to a periodic asymmetric pattern correlates with the ratio of the magnetic strength factor to the structure stiffness C_B/k rather than the magnetic strength factor, which signifies the influence of this ratio on the motion, previously evident from Fig. 12.

A similar insight can be obtained by inspecting the other side of the energy exchange dynamics. Fig. 16 represents the energy exchange characteristics between the flow field and the structure stiffness in the form of $C_l - y$ phase portraits for the three systems at different reduced velocities. This graph provides a tool to assess the energy input to the system from the flow field in the form of work transferred to the moving structure, present in the portraits as the area inside the motion loops. For all systems at $U_r = 4.0$, the curve consists of a single elliptic loop of negligible area, which means that the y and C_l signals are in phase and that a minimal amount of energy is required to sustain the low-amplitude motion. At $U_r = 8.0$, the linear system energy requirements start to increase, but it keeps its pure periodicity. As the square structure enters galloping mode at $U_r = 12.0$ and 14.0, the relationship becomes quasi-periodic, with the system passing through nearly all possible energy states within an envelope. As mentioned above, this envelope represents the extreme states of the flow and potential energy, which are evident when the third field, the kinetic energy, is at its highest value. The monopole system showed similar behavior to an extent, while the stronger dipole magnets showed

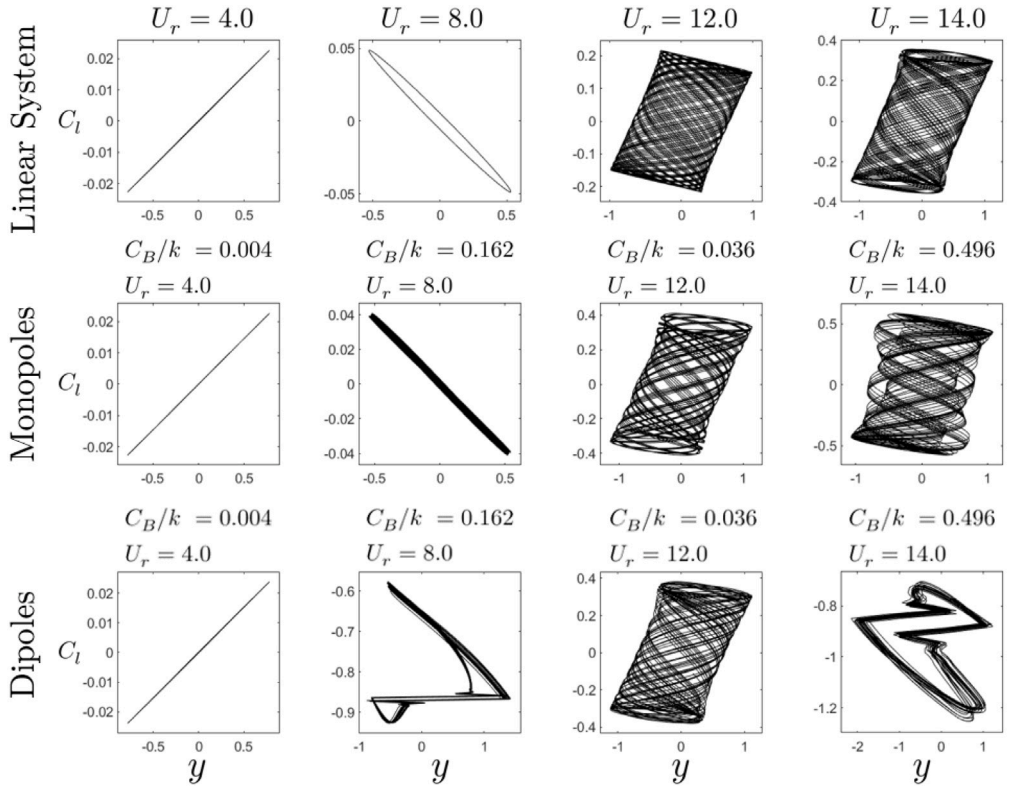


Fig. 16. $C_l - y$ phase portraits for the studied systems for different reduced velocities U_r at $Re = 200$.

chaotic behavior. In contrast, the portraits in the case of the dipole forces at high C_B/k are periodically irregular. This irregular shape proves that the flow forces do not drive the motion, which is now dominated by the two strong repulsive forces that push the system towards a particular potential state regardless of the relatively weaker kinetic and flow energy content.

The effect of the potential energy becomes clear by investigating the effect of the structure's location on the total potential energy. As expected, most structures oscillate around a stable state, represented by a minimum of the potential energy around which the system experiences an increase in the potential energy as it gets further away. This is the case when the energy well of the linear structural stiffness dominates or totally forms the potential energy of the system. This energy well is essential to induce a stable oscillating motion with a periodic single-frequency pattern. The nonlinearity of the potential energy induced by magnetic fields results in deviations that are obvious from Fig. 17. In these cases, the energy well takes another form, as induced by the increasing influence of the magnetic repulsive forces. In some cases, the energy well has two minima, which indicates bistability. Under this condition, the system is expected to *prefer* these positions, such that it does not follow a sinusoidal single-frequency pattern but rather accelerates and decelerates according to its relative location of the dual energy well minima. More notably, the strong influence of the dipole repulsive force at $U_r = 14$ induces an energy well with no minimum. While this cannot be a stable case if the structure is moving independently, the coupling of the two structures ensures that the system as a whole has a stable balanced state, as seen in Fig. 5. The energy characteristics of a single structure result in the behavior noted in the previous discussion. As the system's potential energy requirements to move the same distance or at the same velocity around its stable position are not the same due to the different slopes of the curve, the system moves differently around the stable position.

From this discussion, it becomes clear that the inclusion of a nonlinear force in the dynamics of a galloping system can have complex effects on the vibration response. Under certain conditions, the motion becomes periodic and of a single frequency that can be controlled, regulated, and harnessed through simple systems. Under other conditions, the motion can experience irregularity and distortion or become depressed under the effect of the nonlinear forces, which also represents an opportunity for system control.

4. Conclusions

In this work, the effect of nonlinear magnetically-induced force on the vibration response of two coaxial rods of square cross sections with identical structural parameters at $Re = 200$ and m^*=10 is numerically analyzed. The following points conclude the discussion of this work:

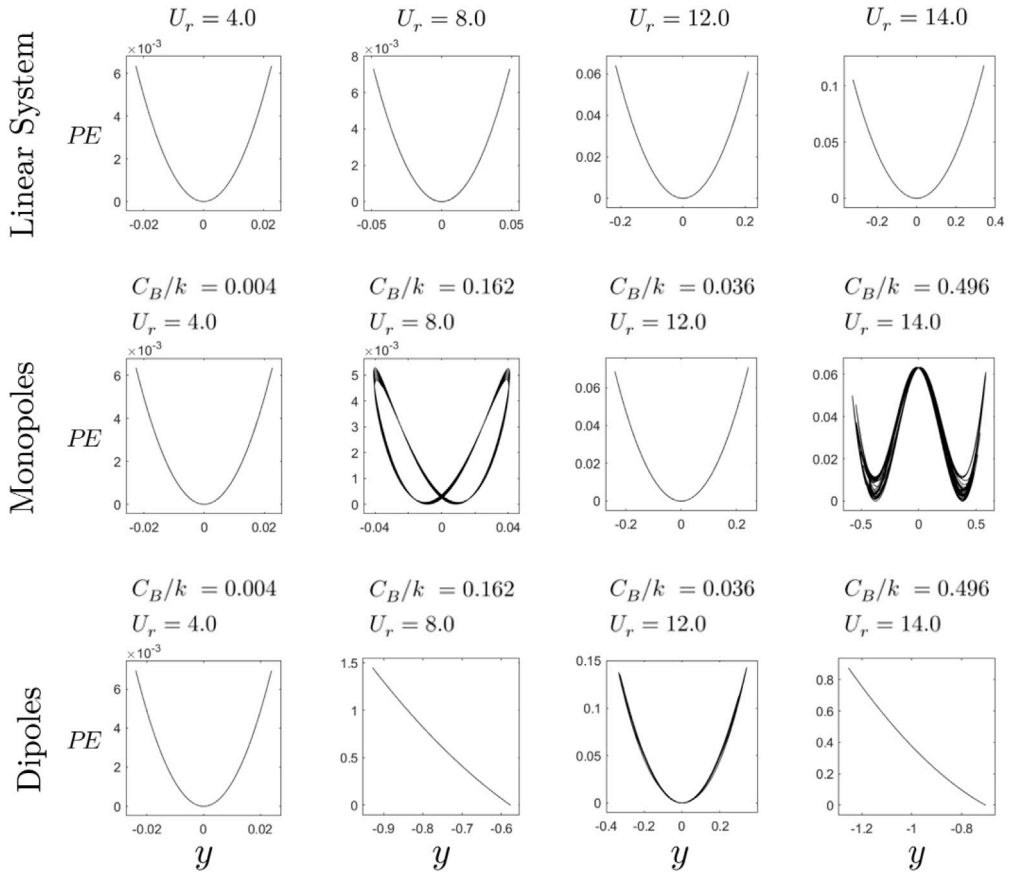


Fig. 17. The total potential energy of a single structure during its motion for different system configurations and reduced flow velocities.

1. The nonlinear repulsion force of two magnetic monopoles, which represent a simplified model for the sides of long, weak magnets, enhances the amplitude of vibration and reduces the onset flow velocity requirements. The improvement at a higher reduced velocity is dependent on the linear contribution of the stiffness added by the magnetic force close to its stability location and thus could be achieved through the use of linear stiffness. This effect has the potential to allow for responsive vibration enhancement by active tweaking of the stiffness closer to the onset velocity.
2. In the case of two magnetic dipoles, the response is a strong function of the magnet strength as a ratio of the structural stiffness. The resulting system is bistable and can be pushed to a more stable state if magnets are sufficiently strong to keep the structures within a potential energy well and maintain the mean distance.
3. The vibration amplitude enhancement is associated with a significant negative added stiffness induced by the repulsion of the magnets. For a pair of dipoles, this negative stiffness correlates with the magnet strength ratio to the structural stiffness, and thus, the vibration amplitude increases linearly with this stiffness ratio. Notably, if the strength of the magnet reaches a limit around $C_B/k = 0.15$, this behavior abruptly stops, and the structures are captured by the more stable state with a mean distance. This can potentially be used as a control mechanism to provide a means for a responsive emergency stop for energy harvesting devices.
4. The vibration frequency of the galloping is not strongly dependent on the magnetic force configuration or strength but rather responds only to changes in the amplitude of the vibration mechanism. Frequencies higher than those for linear stiffness are observed for structures captured within the state with a mean distance, while the enhancement of vibration amplitude is associated with a decrease in the frequency.

Declaration of competing interest

The authors declare that they have no known competing financial interests or personal relationships that could have appeared to influence the work reported in this paper.

Data availability

Data will be made available on request.

References

ASME, 2009. ASME V&V 20 - 2009: Standard for Verification & Validation in Computational Fluid Dynamics & Heat Transfer. The American Society of Mechanical Engineers.

Bearman, P.W., Obasaju, E.D., 1982. An experimental study of pressure fluctuations on fixed and oscillating square-section cylinders. J. Fluid Mech. 119, 297–321. http://dx.doi.org/10.1017/S0022112082001360.

Blevins, R., 1979. Flow-induced vibration in nuclear reactors: A review. Prog. Nucl. Energy 4, 25–49. http://dx.doi.org/10.1016/0149-1970(79)90008-8.

Cao, D., Wang, J., Guo, X., Lai, S.K., Shen, Y., 2022. Recent advancement of flow-induced piezoelectric vibration energy harvesting techniques: Principles, structures, and nonlinear designs. Appl. Math. Mech. 43, 959–978. http://dx.doi.org/10.1007/s10483-022-2867-7.

Carassale, L., Freda, A., Marrè-Brunenghi, M., 2013. Effects of free-stream turbulence and corner shape on the galloping instability of square cylinders. J. Wind Eng. Ind. Aerodyn. 123, 274–280. http://dx.doi.org/10.1016/j.jweia.2013.09.002.

Chen, Z., Tse, K., Kwok, K., Kareem, A., Kim, B., 2021. Measurement of unsteady aerodynamic force on a galloping prism in a turbulent flow: A hybrid aeroelastic-pressure balance. J. Fluids Struct. 102, 103232. http://dx.doi.org/10.1016/j.jfluidstructs.2021.103232.

Chen, S., Zhao, L., 2023. A quasi-zero stiffness two degree-of-freedom nonlinear galloping oscillator for ultra-low wind speed aeroelastic energy harvesting. Appl. Energy 331, 120423. http://dx.doi.org/10.1016/j.apenergy.2022.120423.

Dimitriadis, G., 2017. Introduction to Nonlinear Aeroelasticity. Wiley, http://dx.doi.org/10.1002/9781118756478.

Ding, L., Zhang, L., Bernitsas, M.M., Chang, C.-C., 2016. Numerical simulation and experimental validation for energy harvesting of single-cylinder VIVACE converter with passive turbulence control. Renew. Energy 85, 1246–1259. http://dx.doi.org/10.1016/j.renene.2015.07.088.

Eça, L., Dowding, K., Roache, P.J., 2020. On the interpretation and scope of the V&V 20 standard for verification and validation in computational fluid dynamics and heat transfer. In: ASME 2020 Verification and Validation Symposium. American Society of Mechanical Engineers, http://dx.doi.org/10.1115/VVS2020-8826.

Faltinsen, O.M., 2014. Hydrodynamics of marine and offshore structures. J. Hydrodyn. 26, 835–847. http://dx.doi.org/10.1016/S1001-6058(14)60092-5.

Fujino, Y., Siringoringo, D., 2013. Vibration mechanisms and controls of long-span bridges: A review. Struct. Eng. Int. 23, 248–268. http://dx.doi.org/10.2749/101686613X13439149156886.

Gao, G.-z., Zhu, L.-d., 2017. Nonlinear mathematical model of unsteady galloping force on a rectangular 2:1 cylinder. J. Fluids Struct. 70, 47–71. http://dx.doi.org/10.1016/j.jfluidstructs.2017.01.013.

Guan, M., Liao, W.-H., 2016. Design and analysis of a piezoelectric energy harvester for rotational motion system. Energy Convers. Manage. 111, 239–244. http://dx.doi.org/10.1016/j.enconman.2015.12.061.

Hamlehdar, M., Kasaeian, A., Safaei, M.R., 2019. Energy harvesting from fluid flow using piezoelectrics: A critical review. Renew. Energy 143, 1826–1838. http://dx.doi.org/10.1016/j.renene.2019.05.078.

Han, P., de Langre, E., 2022. There is no critical mass ratio for galloping of a square cylinder under flow. J. Fluid Mech. 931, A27. http://dx.doi.org/10.1017/jfm.2021.975.

He, T., Zhou, D., Bao, Y., 2012. Combined interface boundary condition method for fluid–rigid body interaction. Comput. Methods Appl. Mech. Engrg. 223–224, 81–102. http://dx.doi.org/10.1016/j.cma.2012.02.007.

Hu, G., Liang, J., Tang, L., Wang, J., 2022. Improved theoretical analysis and design guidelines of a two-degree-of-freedom galloping piezoelectric energy harvester. J. Intell. Mater. Syst. Struct. 33, 210–230. http://dx.doi.org/10.1177/1045389X211011681.

Huynh, B., Tjahjowidodo, T., 2017. Experimental chaotic quantification in bistable vortex induced vibration systems. Mech. Syst. Signal Process. 85, 1005–1019. http://dx.doi.org/10.1016/j.ymssp.2016.09.025.

Jafari, M., Hou, F., Abdelkefi, A., 2020. Wind-induced vibration of structural cables. Nonlinear Dynam. 100, 351–421. http://dx.doi.org/10.1007/s11071-020-05541-6.

Joly, A., Etienne, S., Pelletier, D., 2012. Galloping of square cylinders in cross-flow at low Reynolds numbers. J. Fluids Struct. 28, 232–243. http://dx.doi.org/10.1016/j.jfluidstructs.2011.12.004.

Landl, R., 1975. A mathematical model for vortex-excited vibrations of bluff bodies. J. Sound Vib. 42, 219–234. http://dx.doi.org/10.1016/0022-460X(75)90217-5.

Lehner, G., 2010. Electromagnetic Field Theory for Engineers and Physicists. Springer Berlin Heidelberg, Berlin, Heidelberg, http://dx.doi.org/10.1007/978-3-540-76306-2.

Li, X., Lyu, Z., Kou, J., Zhang, W., 2019. Mode competition in galloping of a square cylinder at low Reynolds number. J. Fluid Mech. 867, 516–555. http://dx.doi.org/10.1017/jfm.2019.160.

Liao, P., Fu, J., Ma, W., Cai, Y., He, Y., 2021. Study on the efficiency and dynamic characteristics of an energy harvester based on flexible structure galloping. Energies 14, 6548. http://dx.doi.org/10.3390/en14206548.

Liu, L., Guo, X., Lee, C., 2021. Promoting smart cities into the 5G era with multi-field internet of things (IoT) applications powered with advanced mechanical energy harvesters. Nano Energy 88, 106304. http://dx.doi.org/10.1016/j.nanoen.2021.106304.

Ma, X., Zhou, S., 2022. A review of flow-induced vibration energy harvesters. Energy Convers. Manage. 254, 115223. http://dx.doi.org/10.1016/j.enconman.2022.115223.

Mannini, C., Marra, A., Bartoli, G., 2014. VIV–galloping instability of rectangular cylinders: Review and new experiments. J. Wind Eng. Ind. Aerodyn. 132, 109–124. http://dx.doi.org/10.1016/j.jweia.2014.06.021.

Mannini, C., Massai, T., Marra, A.M., 2018. Modeling the interference of vortex-induced vibration and galloping for a slender rectangular prism. J. Sound Vib. 419, 493–509. http://dx.doi.org/10.1016/j.jsv.2017.12.016.

Mei, X., Zhou, S., Yang, Z., Kaizuka, T., Nakano, K., 2020. A tri-stable energy harvester in rotational motion: Modeling, theoretical analyses and experiments. J. Sound Vib. 469, 115142. http://dx.doi.org/10.1016/j.jsv.2019.115142.

Nakamura, Y., Mizota, T., 1975. Unsteady lifts and wakes of oscillating rectangular prisms. J. Eng. Mech. Div. 101, 855–871. http://dx.doi.org/10.1061/JMCEA3.0002077.

Novak, M., 1972. Galloping oscillations of prismatic structures. J. Eng. Mech. Div. 98, 27–46. http://dx.doi.org/10.1061/JMCEA3.0001575.

Obasaju, E.D., Ermshaus, R., Naudascher, E., 1990. Vortex-induced streamwise oscillations of a square-section cylinder in a uniform stream. J. Fluid Mech. 213, 171. http://dx.doi.org/10.1017/S0022112090002270.

Parkinson, G., 1974. Mathematical models of flow-induced vibrations of bluff bodies: General lecture. In: Flow-Induced Structural Vibrations. Springer Berlin Heidelberg, Berlin, Heidelberg, pp. 81–127. http://dx.doi.org/10.1007/978-3-642-48279-3_9.

Parkinson, G., 1989. Phenomena and modelling of flow-induced vibrations of bluff bodies. Prog. Aerosp. Sci. 26, 169–224. http://dx.doi.org/10.1016/0376-0421(89)90008-0.

Parkinson, G.V., Brooks, N.P.H., 1961. On the aeroelastic instability of bluff cylinders. J. Appl. Mech. 28, 252–258. http://dx.doi.org/10.1115/1.3641663.

Parkinson, G.V., Smith, J.D., 1964. The square prism as an aeroelastic non-linear oscillator. Quart. J. Mech. Appl. Math. 17, 225–239. http://dx.doi.org/10.1093/qjmam/17.2.225.

Roache, P.J., 1997. Quantification of uncertainty in computational fluid dynamics. Annu. Rev. Fluid Mech. 29, 123–160. http://dx.doi.org/10.1146/annurev.fluid.29.1.123.

Sen, S., Mittal, S., 2011. Free vibration of a square cylinder at low Reynolds numbers. J. Fluids Struct. 27, 875–884. http://dx.doi.org/10.1016/j.jfluidstructs.2011.03.006.

Sen, S., Mittal, S., 2015. Effect of mass ratio on free vibrations of a square cylinder at low Reynolds numbers. J. Fluids Struct. 54, 661–678. http://dx.doi.org/10.1016/j.jfluidstructs.2015.01.006.

Sen, S., Mittal, S., 2016. Free vibrations of a square cylinder of varying mass ratios. Procedia Eng. 144, 34–42. http://dx.doi.org/10.1016/j.proeng.2016.05.004.

Shi, M., Holmes, A.S., Yeatman, E.M., 2020. Piezoelectric wind velocity sensor based on the variation of galloping frequency with drag force. Appl. Phys. Lett. 116, http://dx.doi.org/10.1063/5.0012244.

Singh, A.P., De, A.K., Carpenter, V.K., Eswaran, V., Muralidhar, K., 2009. Flow past a transversely oscillating square cylinder in free stream at low Reynolds numbers. Internat. J. Numer. Methods Fluids 61, 658–682. http://dx.doi.org/10.1002/fld.1979.

Smith, B., 1993. A review of dynamic aspects of transmission line design. Eng. Struct. 15, 271–275. http://dx.doi.org/10.1016/0141-0296(93)90030-8.

Sohankar, A., Norberg, C., Davidson, L., 1999. Simulation of three-dimensional flow around a square cylinder at moderate Reynolds numbers. Phys. Fluids 11, 288–306. http://dx.doi.org/10.1063/1.869879.

Sourav, K., Sen, S., 2019. Transition of VIV-only motion of a square cylinder to combined VIV and galloping at low Reynolds numbers. Ocean Eng. 187, 106208. http://dx.doi.org/10.1016/j.oceaneng.2019.106208.

Takashi, N., Hughes, T.J., 1992. An arbitrary Lagrangian-Eulerian finite element method for interaction of fluid and a rigid body. Comput. Methods Appl. Mech. Engrg. 95, 115–138. http://dx.doi.org/10.1016/0045-7825(92)90085-X.

Wanderley, J., Levi, C., 2002. Validation of a finite difference method for the simulation of vortex-induced vibrations on a circular cylinder. Ocean Eng. 29, 445–460. http://dx.doi.org/10.1016/S0029-8018(01)00014-2.

Wang, J.-s., Fan, D., Lin, K., 2020. A review on flow-induced vibration of offshore circular cylinders. J. Hydrodyn. 32, 415–440. http://dx.doi.org/10.1007/s42241-020-0032-2.

Wen, Q., He, X., Lu, Z., Streiter, R., Otto, T., 2021. A comprehensive review of miniatured wind energy harvesters. Nano Mater. Sci. 3, 170–185. http://dx.doi.org/10.1016/j.nanoms.2021.04.001.

Williamson, C., Roshko, A., 1988. Vortex formation in the wake of an oscillating cylinder. J. Fluids Struct. 2, 355–381. http://dx.doi.org/10.1016/S0889-9746(88)90058-8.

Xia, X., Zeng, H., Wang, Z., Zhou, L., Liu, C., 2022. Galloping of two-dimensional section of a marine riser attached with fairing under different inflow angles. Ocean Eng. 260, 112055. http://dx.doi.org/10.1016/j.oceaneng.2022.112055.

Yang, K., Wang, J., Yurchenko, D., 2019. A double-beam piezo-magneto-elastic wind energy harvester for improving the galloping-based energy harvesting. Appl. Phys. Lett. 115, http://dx.doi.org/10.1063/1.5126476.

Yang, Y., Zhao, L., Tang, L., 2013. Comparative study of tip cross-sections for efficient galloping energy harvesting. Appl. Phys. Lett. 102, http://dx.doi.org/10.1063/1.4792737.

Yin, D., Passano, E., Jiang, F., Lie, H., Wu, J., Ye, N., Sævik, S., Leira, B.J., 2022. State-of-the-art review of vortex-induced motions of floating offshore wind turbine structures. J. Mar. Sci. Eng. 10, 1021. http://dx.doi.org/10.3390/jmse10081021.

Yung, K.W., Landecker, P.B., Villani, D.D., 1998. An analytic solution for the force between two magnetic dipoles. Magn. Electr. Separat. 9, 39–52. http://dx.doi.org/10.1155/1998/79537.

Zhang, B., Mao, Z., Song, B., Ding, W., Tian, W., 2018. Numerical investigation on effect of damping-ratio and mass-ratio on energy harnessing of a square cylinder in FIM. Energy 144, 218–231. http://dx.doi.org/10.1016/j.energy.2017.11.153.

Zhao, M., Cheng, L., Zhou, T., 2013. Numerical simulation of vortex-induced vibration of a square cylinder at a low Reynolds number. Phys. Fluids 25, http://dx.doi.org/10.1063/1.4792351.

Zhao, L., Tang, L., Yang, Y., 2014. Enhanced piezoelectric galloping energy harvesting using 2 degree-of-freedom cut-out cantilever with magnetic interaction. Japan. J. Appl. Phys. 53, 060302. http://dx.doi.org/10.7567/JJAP.53.060302.

Zheng, X., He, L., Wang, S., Liu, X., Liu, R., Cheng, G., 2023. A review of piezoelectric energy harvesters for harvesting wind energy. Sensors Actuators A 352, 114190. http://dx.doi.org/10.1016/j.sna.2023.114190.

Zhou, Z., Qin, W., Zhu, P., Shang, S., 2018. Scavenging wind energy by a Y-shaped bi-stable energy harvester with curved wings. Energy 153, 400–412. http://dx.doi.org/10.1016/j.energy.2018.04.035.